

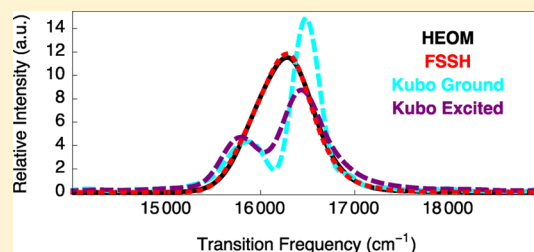
Appraisal of Surface Hopping as a Tool for Modeling Condensed Phase Linear Absorption Spectra

Andrew S. Petit and Joseph E. Subotnik*

Department of Chemistry, University of Pennsylvania, 231 South 34th Street, Philadelphia, Pennsylvania 19104, United States

S Supporting Information

ABSTRACT: Whereas surface hopping is usually used to study populations and mean-field dynamics to study coherences, in two recent papers, we described a procedure for calculating dipole–dipole correlation functions (and therefore absorption spectra) directly from ensembles of surface hopping trajectories. We previously applied this method to a handful of one-dimensional model problems intended to mimic the gas phase. In this article, we now benchmark this new procedure on a set of multidimensional model problems intended to mimic the condensed phase and compare our results against other standard semiclassical methods. By comparison, we demonstrate that methods that include only dynamical information from one PES (the standard Kubo approaches) exhibit large discrepancies with the results of exact quantum dynamics. Furthermore, for model problems with nonadiabatic excited state dynamics but no quantized vibrational structure in the spectra, our surface hopping approach performs comparably to using Ehrenfest dynamics to calculate the electronic coherences. That being said, however, when quantized vibrational structures are present in the spectra but the electronic states are uncoupled, performing the dynamics on the mean PES still outperforms our present method. These benchmark results should influence future studies that use ensembles of independent semiclassical trajectories to model linear as well as multidimensional spectra in the condensed phase.



1. INTRODUCTION

Consider a system described (in the *diabatic* representation) by the Hamiltonian

$$\hat{H} = |g\rangle\hat{H}_g\langle g| + \sum_k |e_k\rangle\hat{H}_{e_k}\langle e_k| + \sum_{k \neq l} |e_k\rangle\hat{V}_{kl}\langle e_l| \quad (1)$$

where \hat{H}_g and $\{\hat{H}_{e_k}\}$ are the nuclear Hamiltonians associated with the ground and excited electronic states, respectively, and the $\{\hat{V}_{kl}\}$ are the diabatic couplings. Note that in eq 1, as well as throughout the article, we will assume that the excited electronic states are all coupled together but no such vibronic coupling exists between the ground state and any of the excited states. The transition dipole moment operator that couples the ground state to the manifold of excited states can be written as

$$\hat{\mu} = \sum_k (|e_k\rangle\hat{\mu}_{eg}\langle g| + |g\rangle\hat{\mu}_{ge_k}\langle e_k|) \quad (2)$$

For such a system at zero temperature, the electronic linear absorption spectrum can be calculated from the Fourier transform of the time-dependent overlap of nuclear wave packets propagated on the ground and excited potential energy surfaces (PESs) according to^{1,2}

$$\alpha(\omega) \propto \omega \text{Re} \left[\int_0^\infty dt e^{i\omega t} \langle \Psi(0) | e^{i\hat{H}t/\hbar} \hat{\mu} e^{-i\hat{H}t/\hbar} \hat{\mu} | \Psi(0) \rangle \right] \quad (3)$$

Here, $|\Psi(0)\rangle = |\chi(0)\rangle|g\rangle$, $|\chi(0)\rangle$ is the initial nuclear wave function, and $e^{-i\hat{H}t/\hbar}|\Psi(0)\rangle$ and $e^{-i\hat{H}t/\hbar}\hat{\mu}|\Psi(0)\rangle$ are wave packets propagated on the ground PES and on the manifold of excited

PESs, respectively. Alternatively, eq 3 can be expressed in terms of the dipole–dipole correlation function, $C_{\mu\mu}(t)$,

$$\begin{aligned} \alpha(\omega) &\propto \omega \text{Re} \left[\int_0^\infty dt e^{i\omega t} \langle \Psi(0) | \hat{\mu}(t) \hat{\mu}(0) | \Psi(0) \rangle \right] \\ &= \omega \text{Re} \left[\int_0^\infty dt e^{i\omega t} C_{\mu\mu}(t) \right] \end{aligned} \quad (4)$$

where $\hat{\mu}(t) = e^{i\hat{H}t/\hbar}\hat{\mu}e^{-i\hat{H}t/\hbar}$. At finite temperatures, the dipole–dipole correlation function can be evaluated from the thermal density matrix $\hat{\rho}_{\text{eq}}$ as

$$C_{\mu\mu}(t) = \text{Im}[\text{Tr}(\hat{\mu}(t)\hat{\mu}(0)\hat{\rho}_{\text{eq}})] \quad (5)$$

Equations 3–5 allow spectral lineshapes to be modeled without first having to calculate a large number of vibrational eigenstates, requiring instead the propagation of nuclear wave packets. In the condensed phase, treating the dynamics of both the electronic and nuclear degrees of freedom quantum mechanically is tractable only for very specific nuclear Hamiltonians and couplings between the nuclei and electrons.^{3,4}

For example, the recently developed hierarchical equations of motion (HEOM) method provides a powerful machinery for calculating numerically exact quantum dynamics provided that the nuclear bath is harmonic with a linear coupling between the electronic and nuclear degrees of freedom.^{5–9}

Given the enormous computational challenges associated with the exact treatment of nuclear quantum dynamics in the

Received: May 29, 2015

condensed phase, a number of semiclassical approaches have been developed to approximate eqs 3–5.^{2–4,10–27} The central idea behind these approaches is to treat the electronic degrees of freedom fully quantum mechanically while approximating the evolving nuclear wave packet with an ensemble of classical trajectories (or frozen gaussians) that are propagated using classical equations of motion. In doing so, the dynamics are usually performed on either the ground PES, as in standard Kubo theory, or on the average of the ground and excited PESs.^{15–18,20,22,28–30} Recently, we proposed an alternative approach in which ensembles of classical trajectories are separately evolved on the ground and on the excited PESs and the dipole–dipole correlation functions independently calculated from these two ensembles are geometrically averaged.³¹ A more detailed description of the semiclassical methods relevant to this study can be found in Section 2.

In the present article, we are interested in methodologies capable of capturing the spectroscopic signatures of non-adiabatic dynamics and electronic relaxation. When the electronic states are coupled, each of the quasi-classical trajectories must be dressed by an electronic wave function that evolves under the time-dependent electronic Schrödinger equation.^{32–35} In Ehrenfest dynamics, the nuclei then evolve on the instantaneous mean-field PES based on the electronic wave function carried by the trajectory.^{36,37} Alternatively, in Tully's fewest switches surface hopping (FSSH), the nuclear equations of motion are derived from a single adiabatic PES. However, the identity of this active adiabatic surface is allowed to vary throughout the simulation through stochastic hops that, within the context of an ensemble of FSSH trajectories, approximate wave packet branching.³² Because of its computational efficiency and algorithmic simplicity, FSSH has become an especially popular theoretical tool for modeling photochemistry and quantifying electronic relaxation branching ratios.^{38–42} Moreover, FSSH has been shown to closely follow detailed balance (as opposed to Ehrenfest dynamics).^{43–45}

Now, with a few exceptions, FSSH has rarely been used to model electronic spectroscopic observables; the method has usually been used to model electronic populations. The exceptions are as follows: First, surface hopping approaches have been used to model the inhomogeneous component of pump–probe signals associated with time-resolved photoelectron spectroscopy, time-resolved absorption, and stimulated Raman spectra.^{46–51} Second, multiple research groups have recently investigated the direct incorporation of the interactions between molecules and strong laser pulses into the FSSH algorithm.^{52–54} Third, Jansen and co-workers recently reported the use of FSSH to propagate electronic populations and Kubo theory to propagate electronic coherences in the simulation of two-dimensional electronic spectra and time-resolved fluorescence.^{55,56} Fourth, Vaníček and co-workers recently reported a study in which they combined their multiple-surface dephasing representation with ensembles of FSSH trajectories in order to calculate linear and time-resolved stimulated emission spectra of pyrazine.⁵⁷ Notwithstanding these exceptions, however, spectroscopy is usually calculated with either ground-state dynamics, excited-state dynamics, or mean-field dynamics.^{2–4,10–27} For example, Jansen has also studied Ehrenfest dynamics for propagating both the populations and electronic coherences associated with two-dimensional electronic spectroscopy.⁵⁸

Recently, we reported methods for calculating the electronic coherences associated with linear absorption and time-resolved differential absorbance spectra directly from ensembles of

FSSH trajectories.^{31,59} These methods were based on identifying the correct mixed quantum-classical nuclear-electronic density matrix associated with a swarm of FSSH trajectories. This density matrix is defined in the spirit of the quantum-classical Liouville equation and uses trajectory information from both the electronic amplitudes and the active adiabatic surfaces to build up the proper nuclear-electronic density matrix.^{30,60–64} Using one-dimensional model problems, we previously demonstrated that our FSSH mixed quantum-classical nuclear-electronic density matrices can be effectively used to propagate spectroscopically relevant electronic coherences in the presence of significant nonadiabatic excited state dynamics.^{31,59} In this article, we extend our analysis to model condensed phase problems as well as to directly compare FSSH versus Ehrenfest for propagating electronic coherences.

We now outline the two major sets of results presented in this article. In Section 2, we will describe several methods that use ensembles of independent semiclassical trajectories to model electronic coherences for uncoupled electronic states (as is relevant for spectroscopy). Our model Hamiltonian consists of two uncoupled electronic states, a harmonic vibrational coordinate that undergoes a large shift upon electronic excitation, a bath of harmonic modes that are weakly effected by the electronic excitation, and bilinear couplings between the system and bath modes on the excited PES. Note that this model Hamiltonian formally requires a Duschinsky rotation to be solved exactly.⁶⁵ Because much of the reorganization energy is concentrated in the system mode, the linear absorption spectra exhibit pronounced quantized vibrational structure, which points to the importance of nuclear wave packet recoherences in the dynamics. In this case, we show that performing dynamics on the mean PES is generally more accurate than averaging together dynamical information obtained from separate swarms of trajectories propagated on the ground and excited PESs. That being said, including dynamical information from only the ground or the excited PES yields spectra with large errors relative to the results of exact quantum dynamics.

In Section 3, we discuss how the semiclassical methods introduced in Section 2 can be generalized to account for coupled electronic states. We then introduce a three-state model Hamiltonian that includes the effects of nonadiabatic excited state dynamics. Each electronic state is coupled to a harmonic bath described by a Drude spectral density, with the reorganization energy distributed evenly among many vibrational modes. Note that these problems can be solved numerically exactly using HEOM.^{5–7} We show that our method (taking the geometric average of electronic coherences calculated from separate swarms of FSSH trajectories propagated on the ground PES and on the excited PES) yields spectra that are comparable to calculating the dipole–dipole correlation function from an ensemble of Ehrenfest trajectories. Both of these methods are shown to be significantly more reliable than the Kubo approaches or including only the inhomogeneous component of the line shape. We conclude in Section 4. Note that we set $\hbar = 1$ throughout this article.

2. LINEAR ABSORPTION SPECTRA IN THE ABSENCE OF ELECTRONIC RELAXATION

2.1. Methods. Perhaps the simplest means of computing an electronic absorption line shape for a condensed phase system is to construct a histogram of the vertical energy gaps sampled by an ensemble of configurations at thermal equilibrium on the ground PES.⁶⁶ If we have a system with two uncoupled

electronic states that satisfies the Condon approximation, then such a histogram can be constructed via

$$\alpha^{(\text{inh})}(\omega) = \frac{4\omega\Delta|\mu_{eg}|^2}{cN_{\text{traj}}} \sum_{l=1}^{N_{\text{traj}}} \frac{1}{(V_e(\vec{x}^{[l]}) - V_g(\vec{x}^{[l]}) - \omega)^2 + \Delta^2/4} \quad (6)$$

where $V_g(\vec{x})$ and $V_e(\vec{x})$ are the PESs for the ground and excited electronic states respectively, μ_{eg} is the transition dipole moment matrix element coupling these electronic states, N_{traj} is the number of configurations in the ensemble, and Δ is a parameter to be discussed below. Equation 6 accounts for the inhomogeneous component of the line shape that physically originates from the distribution of local solvent environments experienced by the chromophore(s). By convoluting each vertical energy gap with a Lorentzian line shape of width Δ , eq 6 phenomenologically accounts for homogeneous broadening.

A popular means of moving beyond the inhomogeneous limit makes use of the formalism originally developed by Kubo^{16,17}

$$C_{\mu\mu}^{(\text{Kubo } g)}(t) = |\mu_{eg}|^2 \langle \exp \left[-\frac{i}{\hbar} \int_0^t (H_e(\vec{x}^{(g)}(t'), \vec{p}^{(g)}(t')) - H_g(\vec{x}^{(g)}(t'), \vec{p}^{(g)}(t'))) dt' \right] \rangle_g \quad (7)$$

where $H_g(\vec{x}, \vec{p})$ and $H_e(\vec{x}, \vec{p})$ are the classical nuclear Hamiltonians for the ground and excited electronic states, the trajectories $\{\vec{x}^{(g)}(t), \vec{p}^{(g)}(t)\}$ are propagated using equations of motion derived from $H_g(\vec{x}, \vec{p})$, and $\langle \dots \rangle_g$ denotes ensemble averaging over initial conditions sampled from the appropriate distribution on the ground PES. Physically, Kubo theory relates the dipole–dipole correlation function to the fluctuating energy gaps sampled by an ensemble of trajectories evolving classically on the ground PES. These fluctuations are caused by both the vibrational motions of the chromophores and the interactions of the chromophores with their environments. Equation 7, therefore, captures not only the inhomogeneous spectral broadening caused by the distribution of local environments but also at least some of the dynamical effects neglected in eq 6.

Although Kubo theory traditionally entails evolving the ensemble of trajectories on the ground PES, eq 7 is readily generalized to allow for propagation on other surfaces. Excited state Kubo, for example, uses an ensemble of trajectories with initial conditions sampled on the ground PES but subsequently evolved on the excited PES

$$C_{\mu\mu}^{(\text{Kubo } e)}(t) = |\mu_{eg}|^2 \langle \exp \left[-\frac{i}{\hbar} \int_0^t (H_e(\vec{x}^{(e)}(t'), \vec{p}^{(e)}(t')) - H_g(\vec{x}^{(e)}(t'), \vec{p}^{(e)}(t'))) dt' \right] \rangle_g \quad (8)$$

Alternatively, the trajectories can be propagated using equations of motion derived from the classical Hamiltonian $H_{(g+e)/2} = H_g/2 + H_e/2$

$$C_{\mu\mu}^{(\text{mean})}(t) = |\mu_{eg}|^2 \times \langle \exp \left[-\frac{i}{\hbar} \int_0^t (H_e(\vec{x}^{((g+e)/2)}(t'), \vec{p}^{((g+e)/2)}(t')) - H_g(\vec{x}^{((g+e)/2)}(t'), \vec{p}^{((g+e)/2)}(t'))) dt' \right] \rangle_g \quad (9)$$

Whereas Kubo theory results from a stochastic and fully classical treatment of environmental fluctuations, the quantum-classical Liouville equation of Kapral and Martens suggests that evolving nuclei on the mean PES, as in eq 9, provides a more accurate semiclassical description of electronic coherences and hence dipole–dipole correlation functions.^{15,18,20,22,28–30}

Recently, we proposed another semiclassical approximation for the dipole–dipole correlation functions associated with electronic linear absorption spectroscopy

$$C_{\mu\mu}^{(\text{SC})}(t) = |\mu_{eg}|^2 \frac{\sqrt{\langle \sigma_{eg}^{(g)}(t) \rangle_g \langle \sigma_{eg}^{(e)}(t) \rangle_g}}{\sigma_{eg}(0)} \\ \langle \sigma_{eg}^{(g)}(t) \rangle = \langle \exp \left[-\frac{i}{\hbar} \int_0^t dt' (H_e(\vec{x}^{(g)}(t'), \vec{p}^{(g)}(t')) - H_g(\vec{x}^{(g)}(t'), \vec{p}^{(g)}(t'))) \right] \rangle_g \sigma_{eg}(0) \\ \langle \sigma_{eg}^{(e)}(t) \rangle = \langle \exp \left[-\frac{i}{\hbar} \int_0^t dt' (H_e(\vec{x}^{(e)}(t'), \vec{p}^{(e)}(t')) - H_g(\vec{x}^{(e)}(t'), \vec{p}^{(e)}(t'))) \right] \rangle_g \sigma_{eg}(0) \quad (10)$$

Here, $\langle \sigma_{eg}^{(g)}(t) \rangle_g$ and $\langle \sigma_{eg}^{(e)}(t) \rangle_g$ are semiclassical approximations to the electronic coherence calculated using ensembles of classical trajectories propagated on the ground and excited PESs, respectively, and $\sigma_{eg}(0)$ is the initial value of the electronic coherence.^{31,59}

Note that this approach effectively combines the dynamical information present in eqs 7 and 8. We previously demonstrated that eq 10 is exact for the case of uncoupled shifted harmonic potentials with identical harmonic frequencies and agrees with the formalism of Kapral and Martens in the short-time limit.³¹

2.2. The Two-State Model and Computational Details.

We consider a model Hamiltonian consisting of two uncoupled electronic states with PESs

$$V_g(\vec{x}) = \frac{m\omega_1^2}{2} x_1^2 + \sum_{k=2}^{N_{\text{modes}}} \frac{m\omega_k^2}{2} x_k^2 \\ V_e(\vec{x}) = \frac{m\omega_1^2}{2} (x_1 - D_1)^2 + \sum_{k=2}^{N_{\text{modes}}} \frac{m\omega_k^2}{2} (x_k - D_k) - \frac{c_k}{m\omega_k^2} (x_1 - D_1)^2 + \epsilon \quad (11)$$

Here, the $\{x_k\}$ are the vibrational normal modes associated with the ground PES. On the excited PES, however, x_1 is treated as a system coordinate that is bilinearly coupled to $N_{\text{mode}} - 1$ bath modes, $\{x_{k>1}\}$. Note that these bilinear couplings between the vibrational modes on the excited PES introduce a Duschinsky rotation so that the normal modes on the ground and excited PESs differ from each other (see Appendix).⁶⁵ As a result, eq 11 is different from two purely shifted harmonic potentials.

In eq 11, we let $m = 1728.26$ au, $\epsilon = 16\,000$ cm^{−1}, $\omega_1 = 500$ cm^{−1}, $N_{\text{modes}} = 100$, and $D_1 = 1/\sqrt{m\omega_1}$ or $D_1 = 2/\sqrt{m\omega_1}$. The displacements in the bath modes on the excited PES, $D_{k>1}$, are all chosen to be much smaller than D_1 ; this physically corresponds to x_1 being much more strongly affected by the electronic excitation than any of the bath modes. The specific values of $D_k\sqrt{m\omega_k}$ were sampled from a Gaussian distribution with a variance of 0.01 and are tabulated in the Supporting Information. The parameters $\omega_{k>1}$ and $c_{k>1}$ are obtained by

discretizing an Ohmic spectral density with an exponential cutoff

$$J(\omega) = \frac{\pi}{2} \sum_{k=1}^N \frac{c_k^2}{m\omega_k} \delta(\omega - \omega_k) = \eta\omega \exp(-\omega/\omega_C) \quad (12)$$

following Craig and Manolopoulos⁶⁷

$$\omega_{k>1} = -\omega_C \ln\left(\frac{k - 3/2}{N_{\text{modes}} - 1}\right)$$

$$c_{k>1} = \omega_k \sqrt{\frac{2\eta m \omega_C}{\pi(N_{\text{modes}} - 1)}} \quad (13)$$

We define, $\omega_C = 1000 \text{ cm}^{-1}$ and $0.01 \leq \eta/m\omega_1 \leq 1.0$. Finally, the transition dipole moment coupling the ground and excited electronic states is assumed to be independent of nuclear position.

The semiclassical calculations were performed using an ensemble of 40 000 trajectories on each surface on which dynamics were performed, for a total of 80 000 trajectories when eq 10 was used. The initial positions and momenta were sampled from the finite temperature harmonic oscillator Wigner distribution associated with the ground PES with $k_B T = 250 \text{ cm}^{-1}$.^{1,68,69} The equations of motion were integrated using the fourth-order Runge–Kutta algorithm with a time step of $\delta t = 0.05 \text{ fs}$.⁷⁰ In doing so, if the energy of a given trajectory drifted significantly within a single time step, then the integration over that time step was repeated using a series of smaller time steps to ensure energy conservation. The sign of the square root in eq 10 is chosen so that $C_{\mu\mu}^{(\text{SC})}(t)$ lies as close as possible in the complex plane to $C_{\mu\mu}^{(\text{SC})}(t - \delta t)$. Numerically exact quantum dynamics calculations were also used to calculate $C_{\mu\mu}(t)$ using a procedure described in the Appendix.

Where applicable, the linear absorption spectra were obtained from $C_{\mu\mu}(t)$ using

$$\alpha(\omega) \simeq -\frac{8\pi\omega}{c\hbar} \text{Im} \left[\int_0^{t_{\text{max}}} e^{i\omega t} \text{Im}[C_{\mu\mu}(t)] \cos\left(\frac{\pi t}{2t_{\text{max}}}\right) dt \right] \quad (14)$$

where the factor $\cos(\pi t/2t_{\text{max}})$ was used to reduce the presence of spurious Gibbs oscillations by forcing the integrand to smoothly go to zero at the final time included in the dynamics, $t_{\text{max}} = 100 \text{ fs}$.⁷¹ The spectra were calculated on a frequency grid with a resolution of 10 cm^{-1} . The inhomogeneous spectral lineshapes were calculated using eq 6 with $\Delta = 250 \text{ cm}^{-1}$ to capture the homogeneous spectral broadening present in the other spectra caused by truncating the Fourier transform in eq 14 at a finite t_{max} . The inhomogeneous spectra were also scaled such that their integrated amplitudes match those of the corresponding spectra calculated using eq 10.

2.3. Results and Discussion. The performance of our approach for the two-state model system described above with $D_1 = 1/\sqrt{m\omega_1}$ or $D_1 = 2/\sqrt{m\omega_1}$ is shown in Figures 1 and 2, respectively. Because $D_1 \gg D_{k>1}$, the spectra exhibit a pronounced Franck–Condon progression in mode x_1 that is broadened due to the bilinear couplings between x_1 and the $\{x_{k>1}\}$ in eq 11 as well as the small displacements in the bath modes. When η is small, the model system is approximately that of uncoupled, displaced harmonic oscillators and eq 10 (red dotted curves) is in quantitative agreement with the results of exact quantum dynamics (black solid curves). As η increases, the semiclassical line shape becomes increasingly broad relative

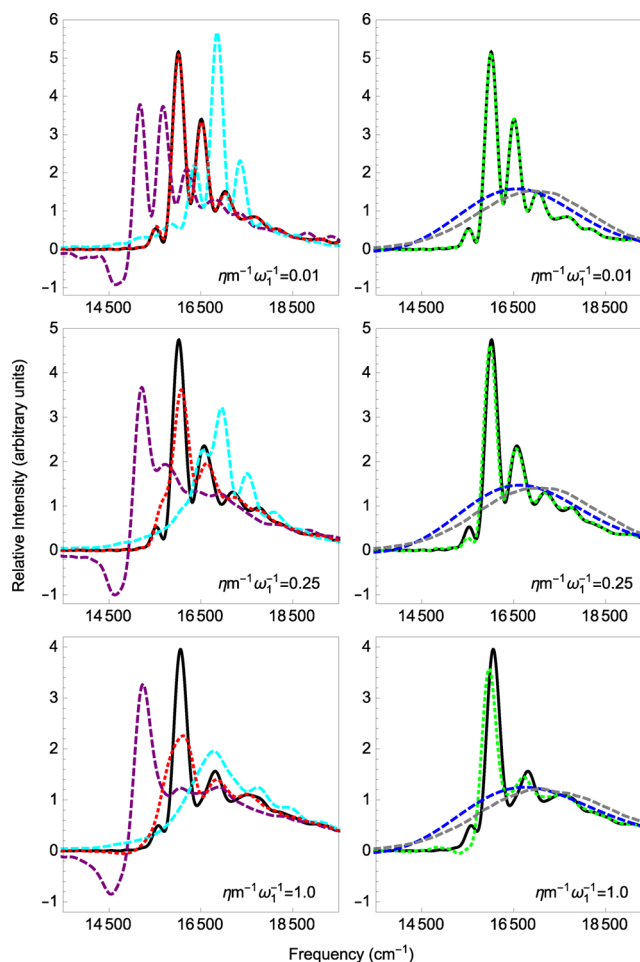


Figure 1. Results of exact quantum dynamics (black solid curves) are compared in the left panels to spectra calculated semiclassically using eq 10 (red dotted curves), ground state Kubo (cyan dashed curves), and excited state Kubo (purple dashed curves). In the right panels, the semiclassical calculations use eq 10 with decoherence included through AFSSH (blue dashed curves), trajectories propagated on the mean PES (green dotted curves), and the inhomogeneous component of the line shape (gray dashed curves). The model systems are defined by eq 11 with $D_1 = 1/\sqrt{m\omega_1}$. Note that the Kubo approaches display qualitatively incorrect lineshapes, the ability of eqs 9 and 10 to capture the quantized vibrational structure present in the spectra decreases with increasing η , and performing dynamics on the mean PES generally outperforms our surface hopping approach.

to the exact results, indicating that our semiclassical description of the electronic coherence decays too quickly. Consistent with our previous work, this results from eq 10 incompletely capturing the effects of the nuclear wave packet recoherences that give rise to the quantized vibrational structure present in the spectra.³¹ The prevalence of nuclear wave packet recoherences in these multidimensional problems reflects the concentration of a significant fraction of the reorganization energy in a single vibrational mode; if we consider the case that, for all $k > 1$, $c_k = 0$ in eq 11, then x_1 carries 30 and 63% of the total reorganization energy for the parameters considered in Figures 1 and 2, respectively. Another signature of these long-lived coherences is that, if we extend t_{max} beyond the bath relaxation time scale, the exact spectral lineshapes continue to narrow significantly. Nevertheless, the spectra calculated using eq 10 contain the correct overall spectral lineshapes and, in

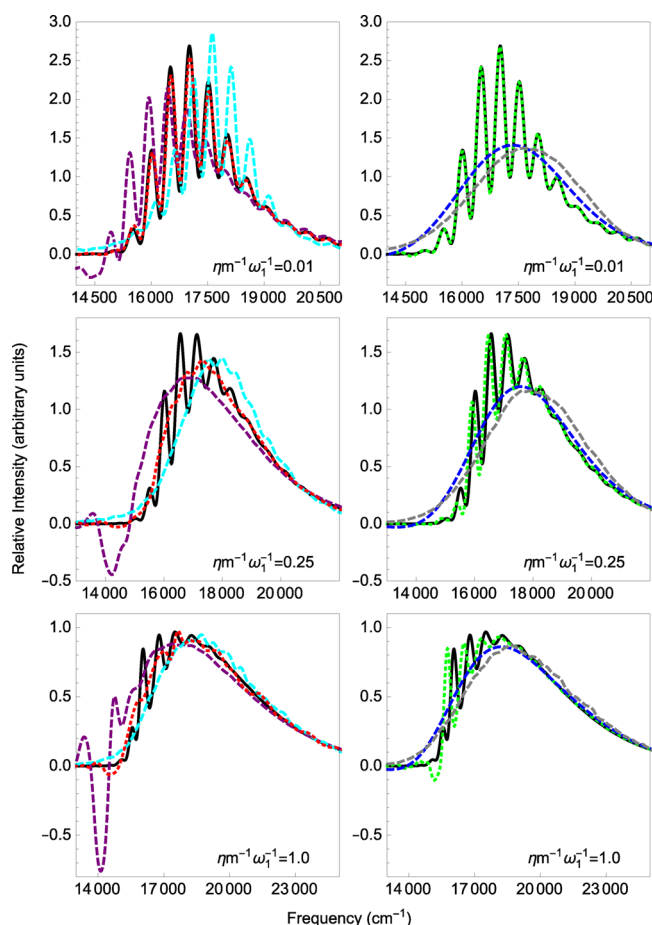


Figure 2. Same data set as Figure 1 except that the reorganization energy is increased by setting $D_1 = 2/\sqrt{m\omega_1}$. Note that the Kubo lineshapes are in better agreement with the exact results (as compared to Figure 1). However, the semiclassical methods that include dynamical information from both surfaces eqs 10 and 9 remain in better agreement with the exact lineshapes than the Kubo methods.

particular for the $D_1 = 1/\sqrt{m\omega_1}$ data, much of the underlying vibrational structure.

Given the discussion of recoherence above, it is perhaps unsurprising that including the effects of decoherence through the augmented fewest switches surface hopping (AFSSH) algorithm (blue dashed curves) gives worse results than not including decoherence at all. The AFSSH algorithm was designed to improve FSSH by estimating the rate of separation between a nuclear wave packet centered on one FSSH trajectory and nuclear wave packets moving on other PESs; the decay of their overlap is accompanied by the decay of the electronic coherences between the states. AFSSH does not consider any recoherence and incorporates decoherence by stochastically and irreversibly collapsing off-diagonal matrix elements of the electronic density matrix. However, true quantum dynamics would have the electronic coherences gradually decay with the separation of the corresponding wave packets and at least partially grow back when the wave packets begin to reapproach each other. As a result, the dipole–dipole correlation functions calculated using AFSSH decay too quickly and the resulting spectra are spuriously broad and lack vibrational structure, behavior similar to that observed in our previous study of one-dimensional model systems.^{59,63,72,73}

Figures 1 and 2 also compare the results of eq 10 to the other semiclassical approximations discussed above. When $D_1 = 1/\sqrt{m\omega_1}$,

both the ground state and excited state Kubo spectra, shown as the cyan dashed and purple dashed curves, respectively, exhibit large, qualitative discrepancies with the exact spectra. Increasing the displacement in the system mode to $D_1 = 2/\sqrt{m\omega_1}$ improves the accuracy of both Kubo approaches (as was also found in our previous work), although the excited state Kubo lineshapes have spurious features at lower frequencies.³¹ Importantly for this article, eq 10 is consistently in better agreement with the exact results than either Kubo approach, indicating the importance of including dynamical information from both PESs involved in the electronic coherence. Similarly, including only the inhomogeneous component of the lineshapes, calculated using eq 6 and shown as the gray dashed curves, results in broad, featureless spectra centered on the ground state Kubo results. Finally, one obvious conclusion from Figures 1 and 2 is that calculating the coherences by performing the dynamics on the mean surface and using eq 9, shown as the green dotted curves, is usually the best approach, especially when η becomes large.

Results shown in the Supporting Information compare eqs 7–10 with their second-order cumulant approximations as well as demonstrate the effect of using classical Boltzmann instead of Wigner initial conditions. As η increases, there is a decrease in the agreement between the spectra calculated using the second-order cumulants and the spectra calculated with the full dipole–dipole correlation functions; the latter are always closer to the exact quantum mechanical results. Using initial conditions sampled from the Boltzmann distribution generally leads to a deterioration in the accuracy of the spectral lineshapes, particularly for large $\eta/m\omega_1$. This reflects the importance of using semiclassical initial conditions when quantized vibrational structure is present in the spectra and $\hbar\omega > k_B T$ ($\hbar\omega_1 = 500 \text{ cm}^{-1}$ while $k_B T = 250 \text{ cm}^{-1}$).³¹

3. LINEAR ABSORPTION SPECTRA WITH ELECTRONIC RELAXATION

3.1. Methods. Throughout this article, we assume that, in the *adiabatic representation*, the transition dipole moment operator is independent of nuclear geometry. Because the adiabatic, $\{|\Phi_i\rangle\}$, and diabatic, $\{|\Xi_a\rangle\}$, electronic bases are related by a unitary transformation that depends on nuclear geometry, $U(\vec{x})$, the Condon approximation will not hold in the *adiabatic representation*. As in our previous studies, we will restrict ourselves to systems in which the excited electronic states are vibronically coupled together but no such vibronic coupling exists between the ground state and any of the excited states.

We focus first on the extension of eq 10 to problems involving excited state nonadiabatic dynamics. In doing so, we will use two swarms of trajectories, one propagated on the ground PES and the other on the manifold of excited PESs using Tully's fewest switches surface hopping algorithm (FSSH).^{32,63,74} For both swarms, the initial nuclear positions and momenta are sampled from the appropriate distribution on the ground PES. As in our previous work, the initial electronic wave function for all of the trajectories (in the *adiabatic representation*) is taken to be a coherent superposition of the ground and all bright states. For example, for a four-state system with diabats 2 and 4 equally bright and diabats 1 and 3 dark, the initial electronic wave function for the l th trajectory is $|\psi^{[l]}(0)\rangle = 1/\sqrt{3}|\Xi_1\rangle + 1/\sqrt{3}|\Xi_2\rangle + 1/\sqrt{3}|\Xi_4\rangle$. Because FSSH dynamics shall be performed in the *adiabatic representation*, we convert to the adiabatic basis using

$$\begin{aligned}
|\psi^{[I]}(0)\rangle &= \sum_a b_a^{[I]}(0) |\Xi_a\rangle \\
&= \sum_i \sum_a U_{ai}(\vec{x}^{[I]}(0)) b_a^{[I]}(0) |\Phi_i\rangle \\
&= \sum_i c_i^{[I]}(0) |\Phi_i\rangle
\end{aligned} \quad (15)$$

We will use $\lambda^{[I]}(t)$ to denote the active adiabatic surface that the nuclei for the I th trajectory are propagated on at time t . For the swarm of trajectories propagated on the excited states, $\lambda^{[I]}(0)$ are stochastically assigned based on $\{lc_k^{[I]}(0)\}^2$.

As in our previous work, the electronic coherence between *adiabats* j and k associated with a swarm of FSSH trajectories is calculated as

$$\langle \sigma_{jk}^{(\text{adiab})}(t) \rangle_g = \frac{1}{N_{\text{traj}}} \sum_{l=1}^{N_{\text{traj}}} \frac{\sigma_{jk}^{[I]}(t)}{\sigma_{jj}^{[I]}(t) + \sigma_{kk}^{[I]}(t)} (\delta_{kl}^{[I]}(t) + \delta_{jl}^{[I]}(t)) \quad (16)$$

where $\sigma_{jk}^{[I]}(t) = c_j^{[I]}(t) c_k^{[I]*}(t)$ is the adiabatic electronic density matrix of the I th trajectory and only trajectories moving along the j th or k th adiabatic PES contribute to the coherence.^{31,59} Note that this definition combines information from both the electronic wave functions carried by the FSSH trajectories and the active adiabatic surfaces that they are propagated on at time t . Similarly, the electronic coherence between *diabats* a and b can be obtained by combining eq 16 with $\mathbf{U}(\vec{x})$

$$\begin{aligned}
\langle \sigma_{ab}^{(\text{diab})}(t) \rangle_g &= \frac{1}{N_{\text{traj}}} \sum_{l=1}^{N_{\text{traj}}} \sum_{jk} U_{aj}(\vec{x}^{[I]}(t)) U_{kb}(\vec{x}^{[I]}(t)) \\
&\times \frac{\sigma_{jk}^{[I]}(t)}{\sigma_{jj}^{[I]}(t) + \sigma_{kk}^{[I]}(t)} (\delta_{kl}^{[I]}(t) + \delta_{jl}^{[I]}(t))
\end{aligned} \quad (17)$$

The dipole–dipole correlation function associated with the two swarms of FSSH trajectories evolved on the ground and on the excited PESs is then calculated as

$$C_{\mu\mu}^{(\text{FSSH})}(t) = \sum_{a>1} |\mu_{a1}^{(\text{diab})}|^2 \frac{\sqrt{\langle \sigma_{a1}^{(\text{diab } g)}(t) \rangle_g \langle \sigma_{a1}^{(\text{diab } e)}(t) \rangle_g}}{\sqrt{\langle \sigma_{a1}^{(\text{diab } g)}(0) \rangle_g \langle \sigma_{a1}^{(\text{diab } e)}(0) \rangle_g}} \quad (18)$$

Here, $\langle \sigma_{a1}^{(\text{diab } g)}(t) \rangle_g$ and $\langle \sigma_{a1}^{(\text{diab } e)}(t) \rangle_g$ are calculated using separate swarms of FSSH trajectories propagated on the ground and excited PESs, respectively, the sum is over all bright diabats, and the denominator ensures proper normalization.

The Kubo approaches as well as the inhomogeneous component of spectral lineshapes are also readily extended to systems with nonadiabatic excited state dynamics. For example, in the *adiabatic representation*, the ground-state Kubo expression for the dipole–dipole correlation function becomes

$$\begin{aligned}
C_{\mu\mu}^{(\text{Kubo } g)}(t) &= \frac{1}{N_{\text{traj}}} \sum_{l=1}^{N_{\text{traj}}} \sum_k \mu_{k1}^{(\text{adiab})}(\vec{x}^{[I]}(t)) \\
&\times \mu_{1k}^{(\text{adiab})}(\vec{x}^{[I]}(0)) \sigma_{k1}^{(\text{Kubo})}(\vec{x}^{[I]}(t)) \\
\mu_{k1}^{(\text{adiab})}(\vec{x}) &= \sum_{a>1} U_{ak}(\vec{x}) \mu_{a1}^{(\text{diab})} \\
\sigma_{k1}^{(\text{Kubo})}(\vec{x}(t)) &= \left[-\frac{i}{\hbar} \int_0^t (E_k(\vec{x}(t')) - E_1(\vec{x}(t'))) dt' \right]
\end{aligned} \quad (19)$$

where $E_k(\vec{x})$ denotes the k th *adiabatic* PES. We use FSSH to propagate the trajectories for excited state Kubo and only include a contribution from the instantaneous active surface at each time step so that

$$\begin{aligned}
C_{\mu\mu}^{(\text{Kubo } e)}(t) &= \frac{1}{N_{\text{traj}}} \sum_{l=1}^{N_{\text{traj}}} \mu_{\lambda^{[I]}(t)1}^{(\text{adiab})}(\vec{x}^{[I]}(t)) \mu_{1\lambda^{[I]}(0)}^{(\text{adiab})}(\vec{x}^{[I]}(0)) \\
&\times \sigma_{\lambda^{[I]}(t)1}^{(\text{Kubo})}(\vec{x}^{[I]}(t))
\end{aligned} \quad (20)$$

Therefore, all differences between the excited state Kubo results and those obtained using eq 18 are due to the procedure used to calculate the dipole–dipole correlation function and not the algorithm used to propagate the dynamics. Similarly, eq 6 becomes

$$\begin{aligned}
\alpha^{(\text{inh})}(\omega) &= \frac{4\omega\Delta}{cN_{\text{traj}}} \sum_{l=1}^{N_{\text{traj}}} \sum_k |\mu_{k1}^{(\text{adiab})}(\vec{x}^{[I]}(t))|^2 \\
&\times \frac{1}{(E_k(\vec{x}^{[I]}) - E_1(\vec{x}^{[I]}) - \omega)^2 + \Delta^2/4}
\end{aligned} \quad (21)$$

Unlike the other semiclassical approaches, eq 9 cannot be directly generalized to problems involving coupled electronic states. However, Ehrenfest dynamics, in which the nuclei evolve on the instantaneous mean-field surface given by

$$E_{\text{Ehr}}(\vec{x}, \vec{c}) = \sum_k |c_k(t)|^2 E_k(\vec{x}(t)) \quad (22)$$

provides a tempting analogue to the mean surface dynamics underlying eq 9. The dipole–dipole correlation associated with a swarm of Ehrenfest trajectories is calculated using

$$\begin{aligned}
C_{\mu\mu}^{(\text{Ehr})}(t) &= \sum_{a>1} |\mu_{a1}^{(\text{diab})}|^2 \frac{\langle \sigma_{a1}^{(\text{diab Ehr})}(t) \rangle_g}{\langle \sigma_{a1}^{(\text{diab Ehr})}(0) \rangle_g} \\
\langle \sigma_{a1}^{(\text{diab Ehr})}(t) \rangle_g &= \frac{1}{N_{\text{traj}}} \sum_{l=1}^{N_{\text{traj}}} \sum_k U_{ak}(\vec{x}^{[I]}(t)) \sigma_{k1}^{[I]}(t)
\end{aligned} \quad (23)$$

3.2. The Three-State Model and Computational Details. We consider a three-state model in which the diabatic PESs are given by

$$\begin{aligned}
V_1(\vec{x}) &= \sum_{k=1}^{N_{\text{modes}}} \frac{m\omega_k^2}{2} x_k^2 \\
V_2(\vec{x}) &= \sum_{k=1}^{N_{\text{modes}}} \frac{m\omega_k^2}{2} (x_k + D_{k,2})^2 + \epsilon_2 \\
V_3(\vec{x}) &= \sum_{k=1}^{N_{\text{modes}}} \frac{m\omega_k^2}{2} (x_k + D_{k,3})^2 + \epsilon_3
\end{aligned} \quad (24)$$

with a constant diabatic coupling, V_{23} , between the two excited states and no such diabatic coupling between the ground state and either excited state ($V_{12} = V_{13} = 0$). In order to facilitate comparison with HEOM calculations, we parametrize the baths by discretizing Drude spectral densities

$$J_a(\omega) = 2\lambda_a \frac{\gamma_a \omega}{\omega^2 + \gamma_a^2} \quad (25)$$

with the bath response frequency $\gamma_a = \gamma = 15 \text{ ps}^{-1}$ for all three states and the bath reorganization energy of the excited states,

$\lambda_{a>1}$, ranging from 250 to 2250 cm^{-1} .⁷ We assume that the density of bath modes can be written as

$$\rho(\omega) = \frac{N_{\text{modes}}}{\arctan(\omega_{\text{max}}/\gamma)} \frac{\gamma}{\omega^2 + \gamma^2} \quad (26)$$

where $\omega_{\text{max}} = 3000 \text{ cm}^{-1}$ is the largest harmonic frequency included in eq 24 and $N_{\text{modes}}/\arctan(\omega_{\text{max}}/\gamma) = \xi$ is a normalization constant. Following Makri, we sample the harmonic frequencies using

$$\int_0^{\omega_k} \rho(\omega) d\omega = k \quad (27)$$

so that $\omega_k = \gamma \tan(k/\xi)$.⁷⁵ Equating the alternative expression for the spectral density

$$J_a(\omega_k) = \frac{\pi}{2} \sum_{k=1}^N \frac{c_{k,a}^2}{m\omega_k} \rho(\omega_k) \quad (28)$$

with eq 25 allows the coupling coefficients to be determined as

$$c_{k,a} = 2\omega_k \sqrt{\frac{\lambda_a m}{\xi \pi}} \quad (29)$$

The displacements used in eq 24 are then obtained as $|D_{k,a}| = c_{k,a}/(m\omega_k^2)$. Note that this discretization scheme corresponds to evenly distributing the reorganization energy among all of the bath modes so that $|D_{k,a}\sqrt{m\omega_k}| \ll 1$ for all of the modes with $\omega_k > 200 \text{ cm}^{-1}$. In order to model uncorrelated system-bath couplings, where each of the electronic states is independently coupled to the bath, we randomly assign the signs of $D_{k,2}$ and $D_{k,3}$ for all of the bath modes. Alternatively, we can model perfectly anticorrelated system-bath couplings, where fluctuations in the bath modes affect the energies of each excited state in exactly opposite ways, by setting $D_{k,2} = -D_{k,3}$ for all of the bath modes.⁷⁶ Finally, the mass of each harmonic oscillator is 1728.26 au and (as stated earlier) the transition dipole moments in the *diabatic representation* are assumed to be position-independent (i.e., the Condon approximation).

Unless specified otherwise, the semiclassical calculations performed using eq 18 employed ensembles with either 30 000 trajectories for each diabatic state if all were bright or 40 000 trajectories for each diabatic state involved in the initial coherence if one of the diabats was dark. The Ehrenfest, Kubo, and inhomogeneous spectral lineshapes were all calculated using ensembles of 40 000 trajectories. The initial positions and momenta were sampled from the finite temperature harmonic oscillator Wigner distribution associated with the ground PES with $T = 300 \text{ K}$ ($k_B T \approx 208 \text{ cm}^{-1}$).^{1,68,69} The equations of motion were integrated using the fourth-order Runge-Kutta algorithm with a time step of $\delta t = 0.025 \text{ fs}$.^{70,77} Where applicable, the spectra were calculated using eq 14 with $t_{\text{max}} = 100 \text{ fs}$ and a frequency grid of 10 cm^{-1} . The parameter Δ in eq 21 was again set to 250 cm^{-1} to account for the homogeneous spectral broadening associated with truncating the Fourier transforms at $t_{\text{max}} = 100 \text{ fs}$. Additionally, we rescale the inhomogeneous line widths so that they have the same integrated amplitudes as the FSSH spectra.

One point of departure from our previous work lies in treating the discontinuities that arise in the numerical evaluation of eq 18 due to the ambiguity in the signs of the square roots.^{31,59} Previously, we ensured the continuity of $C_{\mu\mu}^{(\text{FSSH})}(t)$ by choosing the signs of the square roots in eq 18 such that each lies closest in the complex plane to its value from the previous time step.

Unfortunately, for the model problems considered in this section, this procedure sometimes caused $C_{\mu\mu}^{(\text{FSSH})}(t)$ to be 180° out of phase with the quantum results for portions of the dynamics. As exemplified in Figure 3, this can produce large errors in the final spectral lineshapes.

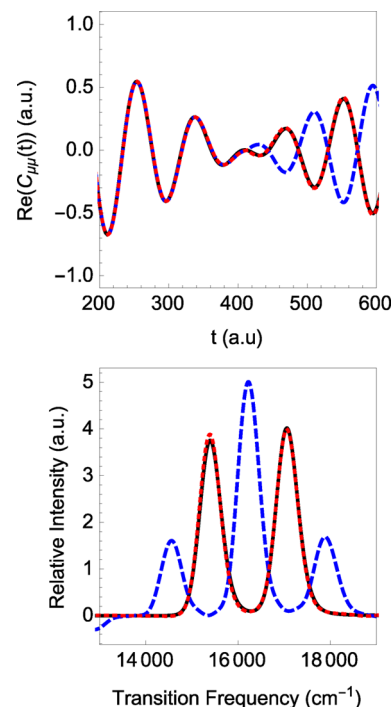


Figure 3. Top panel shows a comparison between dipole–dipole correlation functions calculated using eq 18 and made continuous by either minimizing the distance in the complex plane between $\sqrt{\langle \sigma_{a1}^{(\text{diab } g)}(t) \rangle_g \langle \sigma_{a1}^{(\text{diab } e)}(t) \rangle_g}$ and $\sqrt{\langle \sigma_{a1}^{(\text{diab } g)}(t - \delta t) \rangle_g \langle \sigma_{a1}^{(\text{diab } e)}(t - \delta t) \rangle_g}$ (blue dashed curve) or using the two-step procedure described in this section (red dotted curve). The bottom panel compares the spectra calculated with these dipole–dipole correlation functions. In both panels, the results of HEOM calculations are shown as the black solid curve.

An alternative approach is to (i) require smoothly varying $\sqrt{\langle \sigma_{a1}^{(\text{diab } g)}(t) \rangle_g}$, i.e., choosing the signs that minimize

$$|\sqrt{\langle \sigma_{a1}^{(\text{diab } g)}(t) \rangle_g} - \sqrt{\langle \sigma_{a1}^{(\text{diab } g)}(t - \delta t) \rangle_g}| \quad (30)$$

and (ii) determine the sign of $\sqrt{\langle \sigma_{a1}^{(\text{diab } e)}(t) \rangle_g}$ that lies closest in the complex plane to $\sqrt{\langle \sigma_{a1}^{(\text{diab } g)}(t) \rangle_g}$. We consistently found that this alternative two-step procedure yielded more accurate $C_{\mu\mu}^{(\text{FSSH})}(t)$ for the range of parameters associated with the three-state Hamiltonian (eq 24) considered in this study.

Numerically exact quantum dynamics calculations were performed using HEOM as implemented in the open-source software package PHI.^{5–7} In our calculations, we used a hierarchy truncation level of 17 with time-local truncation and a single Matsubara term.⁸ Note that, due to the requirements of the PHI program, only the excited states were explicitly included in the HEOM calculations; the desired coherences were propagated using the rk4spectrum integrator included in PHI.⁷ Sample PHI input files for the

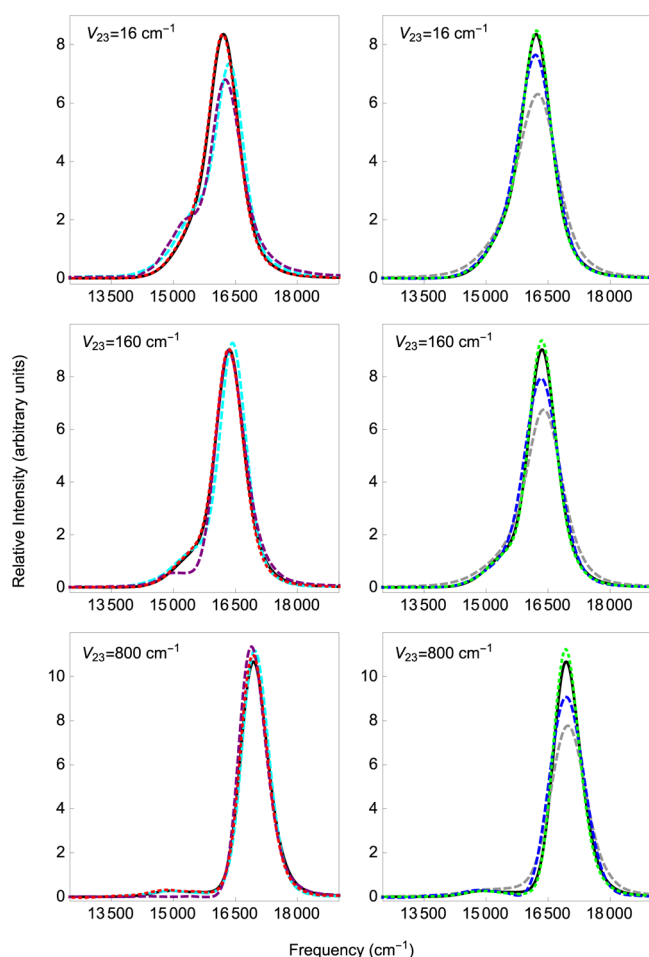


Figure 4. Left panels compare spectra calculated using HEOM (black solid curves) and those calculated semiclassically using eq 18 (red dotted curves), ground state Kubo (cyan dashed curves), and excited state Kubo (purple dashed curves). The right panels compare HEOM (black solid curves) to using eq 18 with AFSSH (blue dashed curves), Ehrenfest (green dotted curves), and the inhomogeneous component of the line shape (gray dashed curves). The results are shown for three-state model systems defined by eq 24 with $\epsilon_2 = 15\,000\text{ cm}^{-1}$, $\epsilon_3 = 16\,000\text{ cm}^{-1}$, $\lambda_2 = 1000\text{ cm}^{-1}$, $\lambda_3 = 250\text{ cm}^{-1}$, uncorrelated system-bath couplings, and both diabats bright. Both the FSSH and Ehrenfest spectra are in excellent agreement with the HEOM results, the inhomogeneous spectral lineshapes are too broad, and the Kubo spectra (particularly excited state Kubo) exhibit deviations from the HEOM results.

calculations reported in this work can be found in the Supporting Information.

3.3. Results and Discussion. Figures 4–7 provide a comparison between the results of applying eqs 17 and 18 (red dotted curves) to the three-state nonadiabatic models discussed above and the results of converged HEOM calculations (black solid curves). Each of these data sets contains a range of diabatic couplings spanning the diabatic and adiabatic limits, with the spectral lineshapes exhibiting a strong dependence on the magnitude of V_{23} . Also illustrated in these figures is how the spectral lineshapes are affected by whether the system-bath couplings are uncorrelated or perfectly anticorrelated as well as whether both excited diabats are equally bright or one is dark. In all cases, the spectra calculated semiclassically using eqs 17 and 18 are in excellent agreement with the HEOM results. Note that doubling the size of t_{\max} in eq 14 does not significantly change the spectral line shapes, indicating that the

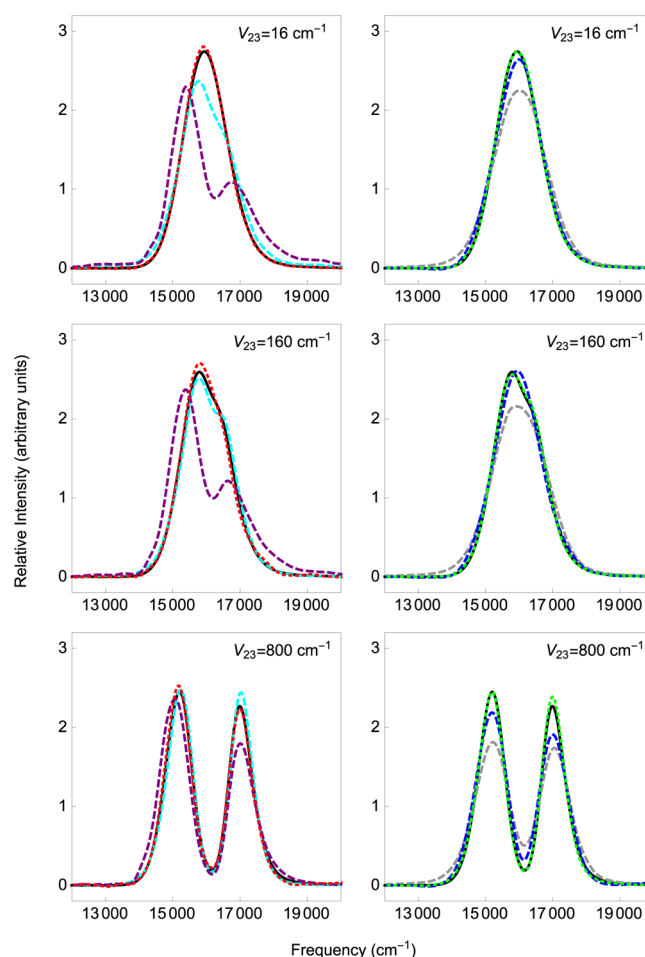


Figure 5. Spectra similar to those in Figure 4 except that diabats 2 and 3 are now dark. Note that the discrepancies between the Kubo and HEOM spectra are more pronounced here relative to Figure 4 where both excited diabats are bright.

line widths are due to the system-bath couplings in eq 24 and not an artifact of truncating the Fourier transforms. A more complete data set containing alternative choices of ϵ_2 , ϵ_3 , λ_2 , and λ_3 can be found in the Supporting Information.

It is worth considering the differences between the two-state models discussed previously in Section 2 and the three-state models described in this section. For the two-state models, one vibrational degree of freedom carries a large fraction of the overall reorganization energy, resulting in the pronounced Franck–Condon progression evident in Figures 1 and 2. Thus, the nuclear dynamics are that of a one-dimensional system perturbed by a bath with significant wave packet recoherences giving rise to the vibrational structure present in the spectra; these wave packet recoherences are especially challenging to model using ensembles of independent semiclassical surface hopping trajectories (see Section 2 and refs 31 and 59). By explicitly treating decoherence but not recoherence, the AFSSH dipole–dipole correlations decay too quickly, resulting in spuriously broad spectra.

Presently, however, for the three-state models considered in this section, the reorganization energy is evenly distributed over all of vibrational modes. With the nuclear dynamics no longer dominated by a single nuclear coordinate, the dynamically relevant regions of phase space are larger and the importance of wave packet recoherences is greatly reduced. As a result, the spectra do not exhibit quantized vibrational structure and eqs 17 and 18 consistently

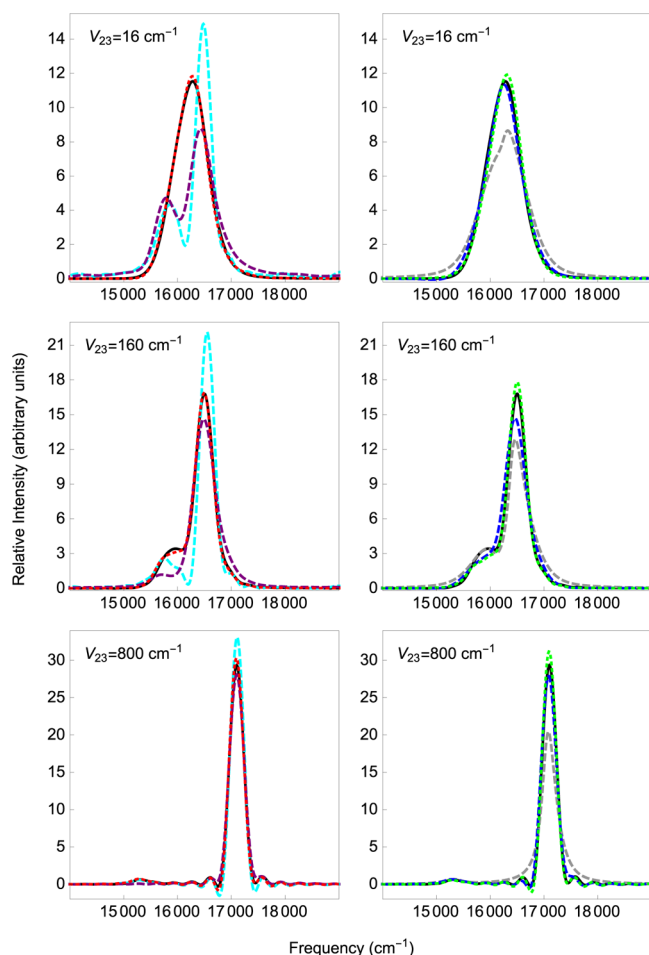


Figure 6. Spectra similar to those in Figure 4 except that $\epsilon_2 = \epsilon_3 = 16\,000\text{ cm}^{-1}$, $\lambda_2 = \lambda_3 = 250\text{ cm}^{-1}$, and there are perfectly anticorrelated system-bath couplings. Note that the discrepancies between the HEOM results and the Kubo and inhomogeneous spectral lineshapes are more pronounced here than in Figure 4 because the system-bath couplings are perfectly anticorrelated (as opposed to uncorrelated).

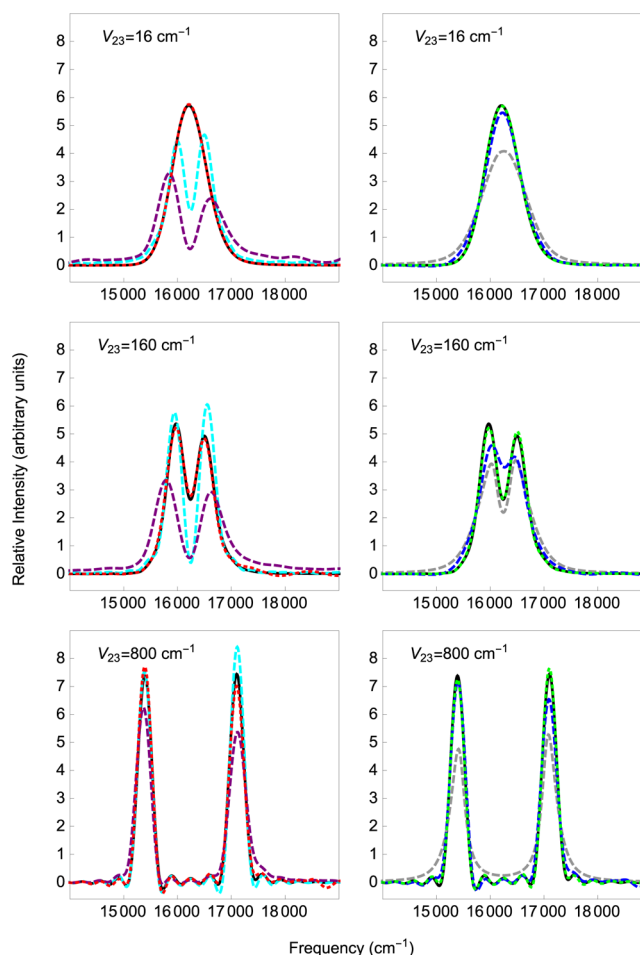


Figure 7. Spectra similar to those in Figure 4 except that $\epsilon_2 = \epsilon_3 = 16\,000\text{ cm}^{-1}$, $\lambda_2 = \lambda_3 = 250\text{ cm}^{-1}$, there are perfectly anticorrelated system-bath couplings, and diabats 3 is dark. Note that the discrepancies between the HEOM results and the Kubo and inhomogeneous spectral lineshapes are more pronounced here than in Figure 4 because the system-bath couplings are perfectly anticorrelated (as opposed to uncorrelated).

provide a good approximation to the coupled electronic and nuclear quantum dynamics, as shown in Figures 4–7.⁷⁸ Regarding decoherence, the AFSSH spectral lineshapes (blue dashed lines) in Figures 4–7 are in much closer accord with the FSSH results than with the two-state model data in Figures 1 and 2; the AFSSH decoherence rates associated with the three-state model are comparable to or only slightly faster than the rates at which the dipole–dipole correlation functions decay due to dephasing.

Figure 8 illustrates the evolution of the *diabatic* excited state populations calculated in the same simulations as were used to generate the spectra in Figures 4 and 5. In the diabatic limit ($V_{23} = 16\text{ cm}^{-1}$), there is little transfer of population between the two excited states. Increasing V_{23} leads to much more significant population transfer, particularly when diabats 3 is dark. Figure 8 also illustrates the ability of FSSH (red curves) and AFSSH (blue curves) to replicate the HEOM results (black curves). When diabats 3 is dark, both FSSH and AFSSH yield population dynamics in good accord with HEOM. However, when both excited diabats are bright, the semiclassical methods display significant errors at long times in both the diabatic and adiabatic limits. Note that when the AFSSH and FSSH results differ, the AFSSH results tend to be in better agreement with the HEOM populations than FSSH.

Figures 4–7 also compare the HEOM results with the other semiclassical methods described above. The spectra calculated using Ehrenfest dynamics with eq 23 (green dotted curves) are found to be comparable with those calculated using FSSH dynamics (eqs 17 and 18), with neither method consistently in better agreement with the HEOM results. Both the ground state Kubo (cyan dashed curves) and the excited state Kubo (purple dashed curves) spectra exhibit large, qualitative errors in the diabatic limit, particularly when the system-bath couplings are perfectly anticorrelated. Increasing V_{23} tends to reduce the deviations between the Kubo and HEOM spectra, with ground state Kubo generally in better agreement with the HEOM results than excited state Kubo when V_{23} is large. However, the magnitude of the errors in the Kubo spectra at intermediate values of V_{23} depends strongly on the other parameters used to define the three-state model. The inhomogeneous spectral lineshapes (gray dashed curves) mirror the ground state Kubo spectra but are consistently too broad, especially when V_{23} is large and/or the system-bath couplings are perfectly anticorrelated.

Finally, before concluding, Figure 9 provides representative data illustrating how the dipole–dipole correlation functions calculated using eqs 17 and 18 converge with the size of the

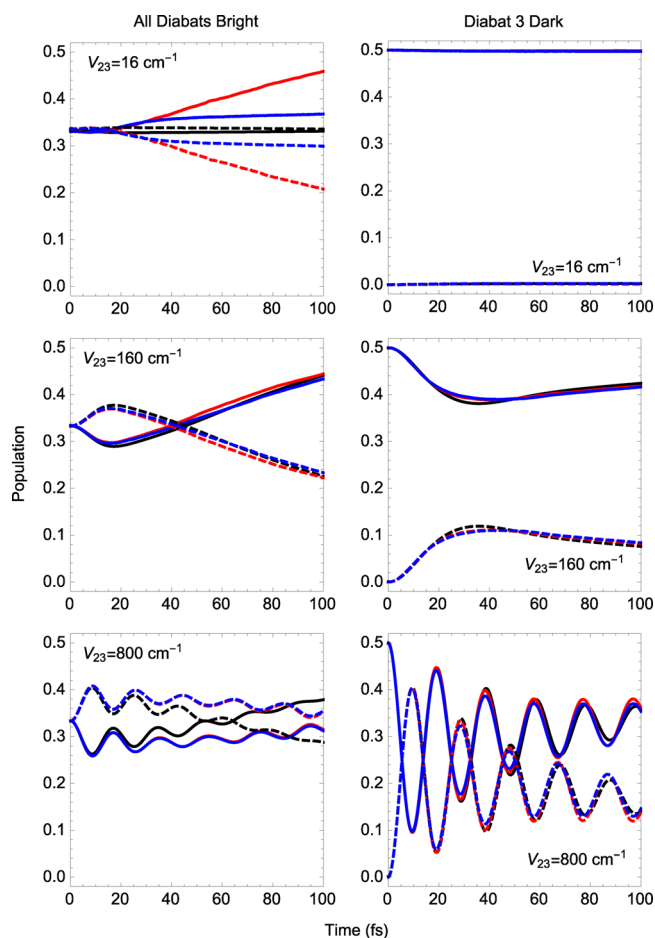


Figure 8. Populations on diabat 2 (solid curves) and diabat 3 (dashed curves) as a function of time calculated using HEOM (black), FSSH (red), and AFSSH (blue). The same simulation parameters were used in as in Figures 4 and 5.

FSSH ensembles. Significant numerical noise is present in the spectra when each of the FSSH ensembles contain only 100 or 500 FSSH trajectories. Increasing the size of the FSSH ensembles to 1000 trajectories eliminates nearly all of the spurious oscillations in the spectra, but some small deviations from the HEOM lineshapes persist. When 5000 trajectories are propagated on the ground and on the excited PESs, the spectra appear to be well-converged, with no significant improvements to the semiclassical lineshapes achieved by increasing the sizes of the FSSH ensembles to 40 000 trajectories per surface.

4. CONCLUSIONS

In this article, we have benchmarked the performance of several methods for modeling electronic coherences and hence spectral lineshapes from ensembles of independent semiclassical trajectories. We focused first on multidimensional problems involving two uncoupled electronic states in which a large fraction of the reorganization energy is concentrated in a single vibrational coordinate that is bilinearly coupled to the other modes on the excited PES. The spectra exhibited pronounced quantized vibrational progressions, indicating that nuclear wave packet recoherences are dynamically significant. We found that performing the dynamics on the mean PES and calculating the electronic coherence using eq 9 is generally more accurate than using eq 10 to average together dynamical information obtained from separate swarms of trajectories evolved on the ground and on the excited

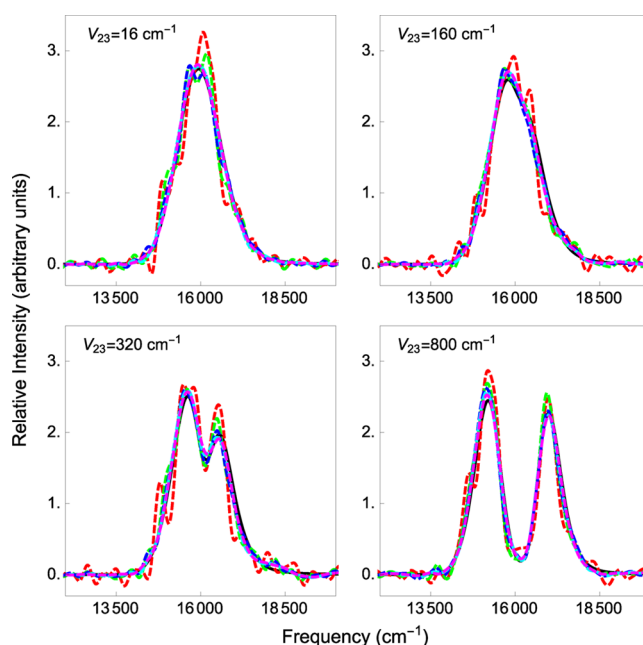


Figure 9. Comparison between results calculated using eq 18 with FSSH ensembles containing (on each active diabats) 100 trajectories (red dashed curves), 500 trajectories (green dashed curves), 1000 trajectories (blue dashed curves), 5000 trajectories (cyan dashed curves), and 40 000 trajectories (magenta dashed curves). The solid black curves show spectra calculated using HEOM. The results shown here are for the model Hamiltonian in Figure 5. Note that the FSSH spectra are well converged when 5000 trajectories are included in each ensemble.

PESs. Use of the AFSSH algorithm resulted in overly broad spectral lineshapes, a reflection of the fact that AFSSH includes decoherence effects but not recoherences. Obviously, one must be careful when using decoherence corrections if one is interested in observables that are directly related to electronic coherences which oscillate significantly before they decay.

Second, we considered three-state model problems that include the effects of excited state nonadiabatic dynamics but with the reorganization energy evenly distributed among a large number of vibrational modes. The resulting spectral lineshapes were devoid of quantized vibrational structure, indicating that nuclear wave packet recoherences were much less important than with the two-state models. Our FSSH method, eqs 17 and 18, performed comparably to using Ehrenfest trajectories (eq 23), and incorporating decoherence through the AFSSH algorithm had only a minor effect on the spectra. We must emphasize that, since quantized vibrational structure is often washed away in condensed phase electronic spectroscopy whereas decoherence can be crucial for dynamics, decoherence corrections for FSSH are almost always beneficial and should be used. For instance, in the present study, AFSSH does improve the calculation of diabatic populations, as is evident in Figure 8.

Using the present data, this comparison between FSSH and Ehrenfest dynamics can be viewed either as a strength or a weakness of our FSSH method. On the one hand, FSSH never outperforms Ehrenfest dynamics for computing complicated coherences, even though FSSH requires more trajectories for convergence. On the other hand, for problems without recoherences and lacking vibrational structure, FSSH performs just as well as Ehrenfest dynamics; concurrently, FSSH finds detailed balance and fully accounts for branching, whereas Ehrenfest dynamics do not.^{43–45} (In all cases, both methods strongly

outperform the ground state Kubo, excited state Kubo, and the inhomogeneous spectral lineshapes.) In general, for predicting populations, the authors are aware of only one numerical study for which Ehrenfest dynamics outperforms FSSH dynamics: surface hopping is a clear improvement over mean-field dynamics when modeling population evolution for transient emission.^{57,79} Thus, there is the temptation to improve the FSSH technology as much as possible; for linear absorption spectroscopy, we believe that we have now reached the limits of the FSSH perspective.

In future studies, it will be interesting to examine more complicated spectral densities and electronic Hamiltonians to identify whether conditions exist where the Ehrenfest and FSSH approaches yield significantly different results, especially because results from harmonic potentials are often not generalizable. It will also be interesting to see where spectroscopic signatures of decoherence become present as well as to develop extensions to the AFSSH algorithm that improve its ability to treat recoherences. Finally, we also plan to investigate the application of the results described here to multidimensional spectroscopy.

■ APPENDIX: Exact Linear Absorption Spectra for Harmonic Potentials with Duschinsky Rotation

We consider a system with two uncoupled electronic states and N vibrational modes with ground and excited nuclear Hamiltonians

$$H_g = \sum_{\alpha=1}^N \frac{p_{\alpha}^2}{2m_{\alpha}} + \frac{m_{\alpha}\omega_{\alpha}^2 x_{\alpha}^2}{2}$$

$$H_e = \sum_{\alpha=1}^N \frac{\tilde{p}_{\alpha}^2}{2\tilde{m}_{\alpha}} + \frac{\tilde{m}_{\alpha}\tilde{\omega}_{\alpha}^2 (\tilde{x}_{\alpha} - \tilde{D}_{\alpha})^2}{2} + \epsilon \quad (31)$$

where the normal modes on the excited PES, \tilde{x}_{α} , are related to those on the ground PES, x_{α} , by a unitary transformation

$$\tilde{x}_{\alpha} = \sum_{k=1}^N L_{\alpha,k} x_k \quad (32)$$

Equation 31 includes the effects of both mode-specific displacements and an overall Duschinsky rotation.⁶⁵ Assuming that the Condon approximation is valid, the dipole–dipole correlation function for this system can be written in the position representation as

$$C_{\mu\mu}(t) = |\mu_{eg}|^2 \int_{-\infty}^{\infty} d\vec{x}' \int_{-\infty}^{\infty} d\vec{x}'' \int_{-\infty}^{\infty} d\vec{x}''' \langle \vec{x}' | \frac{e^{-\hat{H}_g\beta}}{Z} | \vec{x}'' \rangle \times \langle \vec{x}'' | e^{i\hat{H}_g t/\hbar} | \vec{x}''' \rangle \langle \vec{x}''' | e^{-i\hat{H}_e t/\hbar} | \vec{x}' \rangle \quad (33)$$

where $\beta = 1/k_B T$ and Z is the partition function for N uncoupled harmonic oscillators. Because \hat{H}_g is separable in the normal coordinates \vec{x} ,

$$\langle \vec{x}' | \frac{e^{-\hat{H}_g\beta}}{Z} | \vec{x}'' \rangle = \prod_{\alpha=1}^N \langle x'_{\alpha} | \frac{e^{-\frac{1}{2}m_{\alpha}\omega_{\alpha}^2 x_{\alpha}^2}}{Z} | x''_{\alpha} \rangle = \prod_{\alpha=1}^N \sqrt{\frac{m_{\alpha}\omega_{\alpha}(\cosh(\hbar\omega_{\alpha}\beta) - 1)}{\pi\hbar \sinh(\hbar\omega_{\alpha}\beta)}} \times \exp\left[-\frac{m_{\alpha}\omega_{\alpha}}{2\hbar \sinh(\hbar\omega_{\alpha}\beta)}(\cosh(\hbar\omega_{\alpha}\beta) \times (x_{\alpha}'^2 + x_{\alpha}''^2) - 2x_{\alpha}'x_{\alpha}'')\right] \quad (34)$$

and

$$\langle \vec{x}'' | e^{i\hat{H}_g t/\hbar} | \vec{x}''' \rangle = \prod_{\alpha=1}^N \sqrt{\frac{im_{\alpha}\omega_{\alpha}}{2\pi\hbar \sin(\omega_{\alpha}t)}} \times \exp\left[-\frac{im_{\alpha}\omega_{\alpha}}{2\hbar \sin(\omega_{\alpha}t)}(\cos(\omega_{\alpha}t)(x_{\alpha}''^2 + x_{\alpha}'''^2) - 2x_{\alpha}''x_{\alpha}''')\right] \quad (35)$$

where we have used well-known expressions for the Feynman propagator of a one-dimensional harmonic oscillator.^{1,80}

Because the \tilde{x} coordinates are coupled on the excited PES, $\langle \vec{x}''' | e^{-i\hat{H}_e t/\hbar} | \vec{x}' \rangle$ cannot be as easily factored. However, \tilde{x} and \tilde{x}' are related by the unitary transformation given in eq 32 and \hat{H}_e is separable in the \tilde{x} coordinates. We can therefore write

$$\langle \vec{x}''' | e^{-i\hat{H}_e t/\hbar} | \vec{x}' \rangle = \prod_{\alpha=1}^N \langle \tilde{y}_{\alpha}''' | e^{-i\tilde{H}_{\alpha} t/\hbar} | \tilde{y}_{\alpha}' \rangle e^{-i\epsilon t/\hbar}$$

$$= \prod_{\alpha=1}^N \sqrt{\frac{\tilde{m}_{\alpha}\tilde{\omega}_{\alpha}}{2i\pi\hbar \sin(\tilde{\omega}_{\alpha}t)}} \exp\left[\frac{i\tilde{m}_{\alpha}\tilde{\omega}_{\alpha}}{2\hbar \sin(\tilde{\omega}_{\alpha}t)} \times (\cos(\tilde{\omega}_{\alpha}t)(\tilde{y}_{\alpha}'''^2 + \tilde{y}_{\alpha}'^2) - 2\tilde{y}_{\alpha}'''\tilde{y}_{\alpha}')\right] e^{-i\epsilon t/\hbar} \quad (36)$$

where $\tilde{y}_{\alpha} = \tilde{x}_{\alpha} - \tilde{D}_{\alpha}$. Substituting eqs 34–36 into eq 33, using eq 32 to express \tilde{x}_{α} in terms of the x coordinates, and simplifying the resulting expression yields

$$C_{\mu\mu}(t) = \frac{|\mu_{eg}|^2 e^{-i\epsilon t/\hbar}}{2\pi\hbar} \prod_{\alpha=1}^N \sqrt{\frac{m_{\alpha}\omega_{\alpha}(\cosh(\hbar\omega_{\alpha}\beta) - 1)}{\pi\hbar \sinh(\hbar\omega_{\alpha}\beta)}} \times \sqrt{\frac{m_{\alpha}\omega_{\alpha}\tilde{m}_{\alpha}\tilde{\omega}_{\alpha}}{\sin(\omega_{\alpha}t)\sin(\tilde{\omega}_{\alpha}t)}} \exp\left[\frac{i\tilde{m}_{\alpha}\tilde{\omega}_{\alpha}(\cos(\tilde{\omega}_{\alpha}t) - 1)\tilde{D}_{\alpha}^2}{\hbar\sin(\tilde{\omega}_{\alpha}t)}\right] \times \int_{-\infty}^{\infty} d\vec{x}' \int_{-\infty}^{\infty} d\vec{x}'' \int_{-\infty}^{\infty} d\vec{x}''' \times \exp\left[-\sum_{\alpha=1}^N \frac{m_{\alpha}\omega_{\alpha}}{2\hbar \sinh(\hbar\omega_{\alpha}\beta)}(\cosh(\hbar\omega_{\alpha}\beta) \times (x_{\alpha}'^2 + x_{\alpha}''^2) - 2x_{\alpha}'x_{\alpha}'')\right] \times \exp\left[-\sum_{\alpha=1}^N \frac{im_{\alpha}\omega_{\alpha}}{2\hbar \sin(\omega_{\alpha}t)} \times (\cos(\omega_{\alpha}t)(x_{\alpha}''^2 + x_{\alpha}'''^2) - 2x_{\alpha}''x_{\alpha}''')\right] \times \exp\left[-\frac{i}{\hbar} \sum_{k=1}^N \left(\sum_{\alpha=1}^N \frac{\tilde{m}_{\alpha}\tilde{\omega}_{\alpha}(\cos(\tilde{\omega}_{\alpha}t) - 1)\tilde{D}_{\alpha}L_{\alpha,k}}{\sin(\tilde{\omega}_{\alpha}t)}\right) \times (x_k''' + x_k')\right] \times \exp\left[-\frac{i}{\hbar} \sum_{k=1}^N \sum_{l=1}^N \left(\sum_{\alpha=1}^N \frac{\tilde{m}_{\alpha}\tilde{\omega}_{\alpha}L_{\alpha,k}L_{\alpha,l}}{\sin(\tilde{\omega}_{\alpha}t)}\right) x_k'''x_l'\right] \times \exp\left[\frac{i}{2\hbar} \sum_{k=1}^N \sum_{l=1}^N \left(\sum_{\alpha=1}^N \frac{\tilde{m}_{\alpha}\tilde{\omega}_{\alpha}\cos(\tilde{\omega}_{\alpha}t)L_{\alpha,k}L_{\alpha,l}}{\sin(\tilde{\omega}_{\alpha}t)}\right) \times (x_k'''x_l''' + x_k'x_l')\right] \quad (37)$$

The integral over \vec{x}''' can be performed analytically as the product of one-dimensional Gaussian integrals, leading to

$$\begin{aligned}
C_{\mu\mu}(t) = & |\mu_{eg}|^2 e^{-i\epsilon t/\hbar} \prod_{\alpha=1}^N \sqrt{\frac{m_{\alpha}\omega_{\alpha}\tilde{m}_{\alpha}\tilde{\omega}_{\alpha}(\cosh(\hbar\omega_{\alpha}\beta) - 1)}{2\xi_{\alpha}(t)\pi^2\hbar^2\sin(\tilde{\omega}_{\alpha}t)}} \\
& \times \exp\left[\frac{i\tilde{m}_{\alpha}\tilde{\omega}_{\alpha}(\cos(\tilde{\omega}_{\alpha}t) - 1)\tilde{D}_{\alpha}^2}{\hbar\sin(\tilde{\omega}_{\alpha}t)}\right] \\
& \times \int_{-\infty}^{\infty} d\vec{x}' \int_{-\infty}^{\infty} d\vec{x}'' \exp\left[\frac{m_{\alpha}\omega_{\alpha}}{2\hbar\xi_{\alpha}(t)}\left(\frac{\sin(\omega_{\alpha}t)}{\sinh(\hbar\omega_{\alpha}\beta)}x_{\alpha}''\right.\right. \\
& \left.\left.-\frac{\sinh(\hbar\omega_{\alpha}\beta)}{\sin(\omega_{\alpha}t)}x_{\alpha}''^2 + 2ix_{\alpha}''x_{\alpha}'''\right)\right] \times \exp\left[-\sum_{\alpha=1}^N \frac{m_{\alpha}\omega_{\alpha}\cosh(\hbar\omega_{\alpha}\beta)}{2\hbar\sinh(\hbar\omega_{\alpha}\beta)}x_{\alpha}''^2\right] \\
& \times \exp\left[-\sum_{\alpha=1}^N \frac{im_{\alpha}\omega_{\alpha}\cos(\omega_{\alpha}t)}{2\hbar\sin(\omega_{\alpha}t)}x_{\alpha}''^2\right] \\
& \times \exp\left[-\frac{i}{\hbar}\sum_{k=1}^N\left(\sum_{\alpha=1}^N \frac{\tilde{m}_{\alpha}\tilde{\omega}_{\alpha}(\cos(\tilde{\omega}_{\alpha}t) - 1)\tilde{D}_{\alpha}L_{\alpha,k}}{\sin(\tilde{\omega}_{\alpha}t)}\right)(x_k''' + x_k')\right] \\
& \times \exp\left[-\frac{i}{\hbar}\sum_{k=1}^N\sum_{l=1}^N\left(\sum_{\alpha=1}^N \frac{\tilde{m}_{\alpha}\tilde{\omega}_{\alpha}L_{\alpha,k}L_{\alpha,l}}{\sin(\tilde{\omega}_{\alpha}t)}\right)x_k'''x_l'\right] \\
& \times \exp\left[\frac{i}{2\hbar}\sum_{k=1}^N\sum_{l=1}^N\left(\sum_{\alpha=1}^N \frac{\tilde{m}_{\alpha}\tilde{\omega}_{\alpha}\cos(\tilde{\omega}_{\alpha}t)L_{\alpha,k}L_{\alpha,l}}{\sin(\tilde{\omega}_{\alpha}t)}\right)(x_k'''x_l''' + x_k'x_l')\right]
\end{aligned} \quad (38)$$

where $\xi_{\alpha}(t) = \cosh(\hbar\omega_{\alpha}\beta)\sin(\omega_{\alpha}t) + i\cos(\omega_{\alpha}t)\sinh(\hbar\omega_{\alpha}\beta)$.

Our strategy for evaluating the $2N$ dimensional integral in eq 38 is to note that it can be written in the form

$$\begin{aligned}
C_{\mu\mu}(t) = & \mathbb{N}(t) \int d\vec{X} \exp\left[-\frac{1}{2}\vec{X}\cdot\Theta(t)\cdot\vec{X} + \vec{\Gamma}(t)\cdot\vec{X}\right] \\
= & \frac{\mathbb{N}(t)(2\pi)^N}{\sqrt{\det(\Theta(t))}} \exp\left[\frac{1}{2}\vec{\Gamma}(t)\cdot\Theta^{-1}(t)\cdot\vec{\Gamma}(t)\right]
\end{aligned} \quad (39)$$

where \vec{X} is a $2N$ dimensional vector with $X_{k\leq N} = x_k'$ and $X_{k>N} = x_k'''$. The vector $\vec{\Gamma}(t)$ is defined as

$$\Gamma_k(t) = -\frac{i}{\hbar} \sum_{\alpha=1}^{2N} \frac{\tilde{M}_{\alpha}\tilde{\Omega}_{\alpha}\tilde{D}_{\alpha}(\cos(\tilde{\Omega}_{\alpha}t) - 1)\mathbb{L}_{\alpha,k}}{\sin(\tilde{\Omega}_{\alpha}t)} \quad (40)$$

where \mathbb{L} is a block-diagonal $2N$ by $2N$ matrix composed of 2 copies of \mathbb{L} , $\tilde{M}_{k\leq N} = \tilde{M}_{k+N} = \tilde{m}_k$, $\tilde{\Omega}_{k\leq N} = \tilde{\Omega}_{k+N} = \tilde{\omega}_k$, and $\tilde{D}_{k\leq N} = \tilde{D}_{k+N} = \tilde{D}_k$. $\Theta(t)$ is a $2N$ by $2N$ complex symmetric matrix with diagonal elements defined as

$$\begin{aligned}
\Theta_{k,k}(t) = & -\frac{\tilde{M}_k\Omega_k\sin(\Omega_k t)}{\hbar\sinh(\hbar\Omega_k\beta)\Xi_k(t)} + \frac{\tilde{M}_k\Omega_k\cosh(\hbar\Omega_k\beta)}{\hbar\sinh(\hbar\Omega_k\beta)} \\
& -\frac{i}{\hbar}\sum_{\alpha=1}^{2N} \frac{\tilde{m}_{\alpha}\tilde{\Omega}_{\alpha}\cos(\tilde{\Omega}_{\alpha}t)\mathbb{L}_{\alpha,k}^2}{\sin(\tilde{\Omega}_{\alpha}t)}, \quad k \leq N \\
\Theta_{k,k}(t) = & \frac{i\tilde{M}_k\Omega_k\cos(\Omega_k t)}{\hbar\sin(\Omega_k t)} + \frac{\tilde{M}_k\Omega_k\sinh(\hbar\Omega_k\beta)}{\hbar\sin(\Omega_k t)\Xi_k(t)} \\
& -\frac{i}{\hbar}\sum_{\alpha=1}^{2N} \frac{\tilde{m}_{\alpha}\tilde{\Omega}_{\alpha}\cos(\tilde{\Omega}_{\alpha}t)\mathbb{L}_{\alpha,k}^2}{\sin(\tilde{\Omega}_{\alpha}t)}, \quad N < k \leq 2N
\end{aligned} \quad (41)$$

with $\Xi_{k\leq N}(t) = \Xi_{k+N}(t) = \xi_k(t)$. The off-diagonal elements of $\Theta(t)$ that couple x_k' and x_k''' are given by

$$\Theta_{k,l}(t) = -\frac{i\tilde{M}_k\Omega_k}{\hbar\Xi_k(t)} + \frac{i}{\hbar}\sum_{\alpha=1}^{2N} \frac{\tilde{m}_{\alpha}\tilde{\Omega}_{\alpha}\mathbb{L}_{\alpha,k}^2}{\sin(\tilde{\Omega}_{\alpha}t)}, \quad |k-l|=N \quad (42)$$

The off-diagonal elements of $\Theta(t)$ that couple x_k' and x_l' or x_k''' and x_l''' are given by

$$\Theta_{k,l\neq k}(t) = -\frac{i}{\hbar}\sum_{\alpha=1}^{2N} \frac{\tilde{m}_{\alpha}\tilde{\Omega}_{\alpha}\cos(\tilde{\Omega}_{\alpha}t)\mathbb{L}_{\alpha,k}\mathbb{L}_{\alpha,l}}{\sin(\tilde{\Omega}_{\alpha}t)}, \quad |k-l| < N \wedge (k-N)(l-N) > 0 \quad (43)$$

while the off-diagonal elements of $\Theta(t)$ that couple x_k' and x_l''' are given by

$$\Theta_{k,l\neq k}(t) = \frac{i}{\hbar}\sum_{\alpha=1}^{2N} \frac{\tilde{m}_{\alpha}\tilde{\Omega}_{\alpha}\mathbb{L}_{\alpha,k}\mathbb{L}_{\alpha,l}}{\sin(\tilde{\Omega}_{\alpha}t)}, \quad |k-l| > N \quad (44)$$

Finally, the overall prefactor is

$$\begin{aligned}
\mathbb{N}(t) = & |\mu_{eg}|^2 e^{-i\epsilon t/\hbar} \prod_{\alpha=1}^N \sqrt{\frac{m_{\alpha}\omega_{\alpha}\tilde{m}_{\alpha}\tilde{\omega}_{\alpha}(\cosh(\hbar\omega_{\alpha}\beta) - 1)}{2\xi_{\alpha}(t)\pi^2\hbar^2\sin(\tilde{\omega}_{\alpha}t)}} \\
& \times \exp\left[\frac{i\tilde{m}_{\alpha}\tilde{\omega}_{\alpha}(\cos(\tilde{\omega}_{\alpha}t) - 1)\tilde{D}_{\alpha}^2}{\hbar\sin(\tilde{\omega}_{\alpha}t)}\right]
\end{aligned} \quad (45)$$

In evaluating eq 39, it is important to note that $\sqrt{\det(\Theta(t))}$ is generally complex and therefore one must take into account its branch cut. In practice, we found that choosing the root that makes $C_{\mu\mu}(t + \delta t)$ lie closest in the complex plane to $C_{\mu\mu}(t)$ provides a suitable procedure for ensuring that eq 39 yields a continuous dipole–dipole correlation function. Additionally, to maximize numerical stability, we first evaluated $\log(C_{\mu\mu}(t))$ and calculated $\det(\Theta(t))$ through its LU decomposition.⁷⁰

■ ASSOCIATED CONTENT

Supporting Information

The Supporting Information is available free of charge on the ACS Publications website at DOI: 10.1021/acs.jctc.5b00510.

More complete data sets for both the two-state models described by eq 11 and the three-state models described by eq 24; sample input files for the PHI program used to perform the HEOM calculations; examination of the validity of the second-order cumulant approximations to eqs 7–10; comparison between spectra calculated from ensembles of trajectories initialized from classical Boltzmann and semiclassical Wigner distributions; and displacements $D_{k>1}$ used in eq 11 (PDF).

■ AUTHOR INFORMATION

Corresponding Author

*E-mail: subotnik@sas.upenn.edu.

Funding

This material is based upon work supported by the (U.S.) Air Force Office of Scientific Research (USAFOSR) PECASE award under AFOSR grant no. FA9950-13-1-0157. J.E.S. acknowledges a Cottrell Research Scholar Fellowship and a David and Lucille Packard Fellowship.

Notes

The authors declare no competing financial interest.

■ ACKNOWLEDGMENTS

Conversations with Amber Jain were helpful in establishing connections between the model Hamiltonians used in the semiclassical calculations and the parameters used in the HEOM calculations.

REFERENCES

- (1) Tannor, D. J. *Introduction to Quantum Mechanics: A Time Dependent Perspective*; University Science Press: Sausalito, CA, 2007.
- (2) Heller, E. J. *Acc. Chem. Res.* **1981**, *14*, 368–375.
- (3) Nitzan, A. *Chemical Dynamics in Condensed Phases*; Oxford University Press: Oxford, 2006.
- (4) Mukamel, S. *Principles of Nonlinear Optical Spectroscopy*; Oxford University Press: Oxford, 1995.
- (5) Tanimura, Y.; Kubo, R. *J. Phys. Soc. Jpn.* **1989**, *58*, 101.
- (6) Ishizaki, A.; Fleming, G. R. *J. Chem. Phys.* **2009**, *130*, 234111.
- (7) Strümpfer, J.; Schulten, K. *J. Chem. Theory Comput.* **2012**, *8*, 2808–2816.
- (8) Chen, L.; Zheng, R.; Shi, Q.; Yan, Y. *J. Chem. Phys.* **2009**, *131*, 094502.
- (9) Tanimura, Y. *J. Chem. Phys.* **2012**, *137*, 22A550.
- (10) Ben-Nun, M.; Martínez, T. J. *J. Phys. Chem. A* **1999**, *103*, 10517–10527.
- (11) Miller, W. H. *J. Phys. Chem. A* **2001**, *105*, 2942–2955.
- (12) Wang, H.; Thoss, M. *Chem. Phys.* **2004**, *304*, 121–131.
- (13) Shi, Q.; Geva, E. *J. Chem. Phys.* **2005**, *122*, 064506.
- (14) McRobbie, P. L.; Geva, E. *J. Phys. Chem. A* **2009**, *113*, 10425–10434.
- (15) Egorov, S. A.; Rabani, E.; Berne, B. J. *J. Chem. Phys.* **1998**, *108*, 1407–1422.
- (16) Kubo, R. *Adv. Chem. Phys.* **1969**, *15*, 101–127.
- (17) Saven, J. G.; Skinner, J. L. *J. Chem. Phys.* **1993**, *99*, 4391–4402.
- (18) Shemetulskis, N. E.; Loring, R. F. *J. Chem. Phys.* **1992**, *97*, 1217–1226.
- (19) Spencer, C.; Loring, R. F. *J. Chem. Phys.* **1996**, *105*, 6596–6606.
- (20) Mukamel, S. *J. Chem. Phys.* **1982**, *77*, 173–181.
- (21) Wehrle, M.; Šulc, M.; Vaníček, J. *Chimia* **2011**, *65*, 334–338.
- (22) Šulc, M.; Hernández, H.; Martínez, T. J.; Vaníček, J. *J. Chem. Phys.* **2013**, *139*, 034112.
- (23) Webster, F.; Schnitker, J.; Friedrichs, M. S.; Friesner, R. A.; Rossky, P. J. *Phys. Rev. Lett.* **1991**, *66*, 3172.
- (24) Turi, L.; Hantal, G.; Rossky, P. J.; Borgis, D. *J. Chem. Phys.* **2009**, *131*, 024119.
- (25) Kühn, O.; Makri, N. *J. Phys. Chem. A* **1999**, *103*, 9487–9493.
- (26) Reik, N.; Hsieh, C.-Y.; Freedman, H.; Hanna, G. *J. Chem. Phys.* **2013**, *138*, 144106.
- (27) Hanna, G.; Geva, E. *J. Phys. Chem. B* **2011**, *115*, 5191–5200.
- (28) Egorov, S. A.; Rabani, E.; Berne, B. J. *J. Chem. Phys.* **1999**, *110*, 5238–5248.
- (29) Bursulaya, B. D.; Kim, H. J. *J. Phys. Chem.* **1996**, *100*, 16451–16456.
- (30) Kapral, R.; Ciccotti, G. *J. Chem. Phys.* **1999**, *110*, 8919–8929.
- (31) Petit, A. S.; Subotnik, J. E. *J. Chem. Phys.* **2014**, *141*, 014107.
- (32) Tully, J. C. *J. Chem. Phys.* **1990**, *93*, 1061–1071.
- (33) Stock, G.; Thoss, M. *Phys. Rev. Lett.* **1997**, *78*, 578–581.
- (34) Ben-Nun, M.; Quenneville, J.; Martínez, T. J. *J. Phys. Chem. A* **2000**, *104*, 5161–5175.
- (35) Miller, W. H. *J. Phys. Chem. A* **2009**, *113*, 1405–1415.
- (36) McLachlan, A. D. *Mol. Phys.* **1964**, *8*, 39–44.
- (37) Meyer, H. D.; Miller, W. H. *J. Chem. Phys.* **1980**, *72*, 2272–2281.
- (38) Jones, G. A.; Carpenter, B. K.; Paddon-Row, M. N. *J. Am. Chem. Soc.* **1998**, *120*, 5499–5508.
- (39) Hazra, A.; Soudackov, A. V.; Hammes-Schiffer, S. *J. Phys. Chem. B* **2010**, *114*, 12319–12332.
- (40) Nachtigallová, D.; Aquino, A. J. A.; Szymczak, J. J.; Barbatti, M.; Hobza, P.; Lischka, H. *J. Phys. Chem. A* **2011**, *115*, 5247–5255.
- (41) Granucci, G.; Persico, M. *J. Chem. Phys.* **2007**, *126*, 134114.
- (42) Fernandez-Alberti, S.; Kleiman, V. D.; Tretiak, S.; Roitberg, A. E. *J. Phys. Chem. A* **2009**, *113*, 7535–7542.
- (43) Parandekar, P. V.; Tully, J. C. *J. Chem. Phys.* **2005**, *122*, 094102.
- (44) Parandekar, P. V.; Tully, J. C. *J. Chem. Theory Comput.* **2006**, *2*, 229–235.
- (45) Schmidt, J. R.; Parandekar, P. V.; Tully, J. C. *J. Chem. Phys.* **2008**, *129*, 044104.
- (46) Sheu, W. S.; Rossky, P. J. *Chem. Phys. Lett.* **1993**, *213*, 233–238.
- (47) Schwartz, B. J.; Rossky, P. J. *J. Chem. Phys.* **1994**, *101*, 6917–6926.
- (48) Mitrić, R.; Werner, U.; Bonačić-Koutecký, V. *J. Chem. Phys.* **2008**, *129*, 164118.
- (49) Humeniuk, A.; Wohlgemuth, M.; Suzuki, T.; Mitrić, R. *J. Chem. Phys.* **2013**, *139*, 134104.
- (50) Dorfman, K. E.; Fingerhut, B. P.; Mukamel, S. *Phys. Chem. Chem. Phys.* **2013**, *15*, 12348–12359.
- (51) Fingerhut, B. P.; Dorfman, K. E.; Mukamel, S. *J. Chem. Theory Comput.* **2014**, *10*, 1172.
- (52) Mitrić, R.; Petersen, J.; Bonačić-Koutecký, V. *Phys. Rev. A: At, Mol., Opt. Phys.* **2009**, *79*, 053416.
- (53) Richter, M.; Marquetand, P.; González-Vázquez, J.; Sola, I.; González, L. *J. Chem. Theory Comput.* **2011**, *7*, 1253–1258.
- (54) Bajo, J. J.; González-Vázquez, J.; Sola, I. R.; Santamaria, J.; Richter, M.; Marquetand, P.; González, L. *J. Phys. Chem. A* **2012**, *116*, 2800–2807.
- (55) Tempelaar, R.; van der Vegte, C. P.; Knoester, J.; Jansen, T. L. *C. J. Chem. Phys.* **2013**, *138*, 164106.
- (56) Tempelaar, R.; Spano, F. C.; Knoester, J.; Jansen, T. L. *C. J. Phys. Chem. Lett.* **2014**, *5*, 1505–1510.
- (57) Zimmermann, T.; Vaníček, J. *J. Chem. Phys.* **2014**, *141*, 134102.
- (58) van der Vegte, C. P.; Dijkstra, A. G.; Knoester, J.; Jansen, T. L. *C. J. Phys. Chem. A* **2013**, *117*, 5970–5980.
- (59) Petit, A. S.; Subotnik, J. E. *J. Chem. Phys.* **2014**, *141*, 154108.
- (60) Martens, C. C.; Fang, J. Y. *J. Chem. Phys.* **1997**, *106*, 4918–4930.
- (61) Donoso, A.; Martens, C. C. *J. Phys. Chem. A* **1998**, *102*, 4291–4300.
- (62) Nielsen, S.; Kapral, R.; Ciccotti, G. *J. Chem. Phys.* **2000**, *112*, 6543–6553.
- (63) Subotnik, J. E.; Ouyang, W.; Landry, B. R. *J. Chem. Phys.* **2013**, *139*, 214107.
- (64) Landry, B. R.; Falk, M. J.; Subotnik, J. E. *J. Chem. Phys.* **2013**, *139*, 211101.
- (65) Duschinsky, F. *Acta. Physicochimica. U.S.S.R.* **1937**, *7*, 551.
- (66) Marini, A.; Muñoz Losa, A.; Biancardi, A.; Mennucci, B. *J. Phys. Chem. B* **2010**, *114*, 17128–17135.
- (67) Craig, I. R.; Manolopoulos, D. E. *J. Chem. Phys.* **2005**, *122*, 084106.
- (68) Wigner, E. *Phys. Rev.* **1932**, *40*, 749–759.
- (69) Case, W. B. *Am. J. Phys.* **2008**, *76*, 937–946.
- (70) Press, W.; Flannery, B.; Teukolsky, S.; Vetterling, W. *Numerical Recipes in FORTRAN: The Art of Scientific Computing*; Cambridge University Press: Cambridge, 1992.
- (71) Worth, G. A.; Meyer, H.-D.; Cederbaum, L. S. In *Conical Intersections: Electronic Structure, Dynamics, and Spectroscopy*; Domcke, W., Yarkony, D. R., Köppel, H., Eds.; World Scientific Publishing Co. Pte. Ltd.: Hackensack, NJ, 2004; Chapter 14, pp 619–698.
- (72) Landry, B. R.; Subotnik, J. E. *J. Chem. Phys.* **2012**, *137*, 22A513.
- (73) For the present two-state model where there are no derivative couplings, the AFSSH decoherence rate is calculated as $1/\tau_{\text{decoher}} = \Delta\vec{F} \cdot \Delta\vec{R} / 2\hbar$, where $\Delta\vec{F}$ is the difference in forces between the two PESs and $\Delta\vec{R}$ estimates the spatial distance between the trajectory and the center of a wave packet moving on the other PES. Thus, the decoherence rate is large when the two PESs have very different forces, causing wave packets moving on the two surfaces to rapidly drift apart and hence their overlap decay to zero.
- (74) Tully, J. C. *Faraday Discuss.* **1998**, *110*, 407–419.
- (75) Makri, N. *J. Phys. Chem. B* **1999**, *103*, 2823–2829.
- (76) Strümpfer, J.; Schulten, K. *J. Chem. Phys.* **2011**, *134*, 095102.
- (77) During the integration of the nuclear equations of motion, if the energy of a trajectory drifted significantly within a single time step, then the integration over that time step was repeated using a series of smaller time steps to ensure energy conservation. Before evolving the wave function, we identified $h\nu_{\text{max}}$ as the largest electronic Hamiltonian matrix element appearing in the time-dependent Schrödinger equation. If $(10\nu_{\text{max}})^{-1} > \delta t$, then the time-dependent electronic Schrödinger equation was integrated from t to $t + \delta t$ over a series of

smaller time steps of length $(10\nu_{\max})^{-1}$. In doing so, the nuclear velocity, derivative couplings, and adiabatic electronic energies were linearly interpolated from their values at t to their values at $t + \delta t$. Note that regardless of the size of $(10\nu_{\max})^{-1}$, we only considered hops between the electronic states at the end of the full time step at $t + \delta t$.

(78) Sampling initial conditions from the classical Boltzmann distribution instead of the semiclassical Wigner distribution does lead to a small narrowing of the spectral lineshapes, but the effect is much more subtle than that observed with the two-state models (see [Supporting Information](#)). This is consistent with the fact that all of the modes with large $|D_{k,d}|$ have $\hbar\omega_k < k_{\text{B}}T$.

(79) Kohen, D.; Stillinger, F. H.; Tully, J. C. *J. Chem. Phys.* **1998**, *109*, 4713–4725.

(80) Barone, F. A.; Boschi-Filho, H.; Farina, C. *Am. J. Phys.* **2003**, *71*, 483.